A Simple Technique Linearizing and Decoupling DC-Link Voltage Control From Source Nonlinearity in Single-Stage Photovoltaic Inverters

Leonardo Callegaro, *Member, IEEE*, Foad Taghizadeh, *Senior Member, IEEE*,
Sara Deilami, *Senior Member, IEEE*, and Mihai Ciobotaru, *Senior Member, IEEE*

***Abstract*—The nonlinear behavior of photovoltaic (PV) sources can deteriorate the performance of PV inverters if their control system is not designed carefully. This article investigates the PV source influence on the dc voltage regulation of single-stage single-phase grid-connected inverters. The analysis reveals two issues: undesired strong coupling between regulation transient performance and PV source operating point, and possible instability arising when the PV source operates on the left-hand side of its maximum power point (MPP). To eradicate these issues, the idea to add the PV power feedforward signal to the output of the dc voltage controller is applied. This action cancels the nonlinearity induced by the source, responsible for poor PV voltage regulation performance, resulting in large-signal linear and stable dc voltage control dynamics. The benefit is twofold. First, the dc voltage transient response is desirably decoupled from the PV source operating condition (left-hand side of MPP, MPP, and right-hand side of MPP). Second, the possible instability occurring at the left-hand side of the MPP is eliminated. The research findings are supported by simulations and experimental results extracted out of a grid-connected inverter fed by a PV emulator. Through this testbed, the proposed controller is compared against conventional and emerging dc voltage control schemes.**

***Index Terms*—Cascaded control, dc–ac power conversion, photovoltaic (PV) power systems, photovoltaic voltage control, transient response.**

I. INTRODUCTION

RENEWABLES proliferation is leading to a paradigm shift in the electric power system, where the majority of energy sources will be connected via power electronic converters and, commonly, inverters. These devices operate with control algorithms enabling the energy transfer from the primary source, e.g., solar photovoltaic (PV) and wind, to the electricity network, in compliance with grid codes [1]. Technical standards, such as [2], [3], [4], and [5], prescribe rules that converters must comply with to support grid voltage and frequency regulation. Some of these rules demand that a converter shall curtail its power output during grid overvoltage or overfrequency events. In other words, renewable interfacing converters must be able to reduce their power injection when necessary, rather than uniquely operate at full power output.

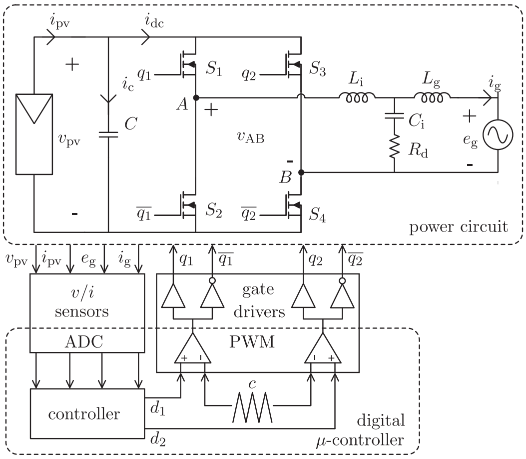

Fig. 1. Single-stage single-phase PV inverter power and control stages.

PV interfacing converters, of interest to this work (see Fig. 1), typically control their input voltage to extract power from the PV source, utilizing a maximum power point tracking (MPPT) algorithm. Power reduction according to grid code requirements is achieved by moving the quiescent point of the PV source away from the maximum power point (MPP), either to its left-hand side or to its right-hand side [6], [7]. Besides, fast-changing solar irradiance can also involuntarily cause operation away from the MPP [8], [9]. It is natural to ask whether this operating condition affects the dynamic performance and stability of the PV interfacing converter. The answer reveals possible issues; in [10] and [11], the input voltage regulation of a boost converter is shown to depend undesirably on the operating point of the PV source, with damping decreasing from the right-hand side to the left-hand side of the MPP. Similar considerations are drawn in [12] and[13] for PV interfacing buck and noninverting buck–boost converters. Like in [10], [11], [12], and [13], in [14], the behavior of several dc–dc and dc–ac converters is shown to

---

Manuscript received 7 February 2023; revised 5 May 2023; accepted 19 June 2023. Date of publication 30 June 2023; date of current version 28 July 2023. This work was supported by Macquarie University under Grant MQRAS-2022. Recommended for publication by Associate Editor D. Xu. *(Corresponding author: Leonardo Callegaro.)*

Leonardo Callegaro, Foad Taghizadeh, and Sara Deilami are with the School of Engineering, Macquarie University, Sydney, NSW 2109, Australia (e-mail: leonardo.callegaro@mq.edu.au; foad.taghizadeh@mq.edu.au; sara.deilami@mq.edu.au).

Mihai Ciobotaru is with the EcoJoule Energy, Brisbane, QLD 4129, Australia (e-mail: ciomih@ieee.org).

Color versions of one or more figures in this article are available at https://doi.org/10.1109/TPEL.2023.3290958.

Digital Object Identifier 10.1109/TPEL.2023.3290958

be challenged by the *dynamic resistance*, an internal parameter of the PV source, whose high variability is the cause of possible instability on the left-hand side of the MPP. The relation between PV source operating point and stability of three-phase voltage source inverters (VSI's) is assessed in [15], [16], and [17], with the purpose to reduce the size of the converter input capacitance; dc-side stability of current source inverters is studied in [18], by means of an accurate although rather involved model. While the cited references consolidate the knowledge of issues related to PV interfacing converters operating away from the MPP, they mostly deal with dc–dc converters or three-phase inverters, and treat the case where the controlled variable is the PV voltage; also, not all of them validate their findings with experimental results. The literature is lacking analysis on the stability of PV voltage regulation in single-phase VSI's, when the control variable is the square of the PV voltage, a control scheme commonly found in practice [19, p. 189], but rarely scrutinized. Closing this gap, this article investigates the PV voltage regulation stability of current-controlled single-phase VSI's, like the one shown in Fig. 1, where dc-link regulation is achieved by controlling the square of the PV voltage. The purpose is to identify the pitfalls of traditional controller design based on small-signal transfer functions, eliciting the conditions leading to instability when the PV source works on the left-hand side of the MPP. To eliminate the issues identified, it is proposed to add the PV power feedforward signal to the output of the voltage controller. This action effectively provides a linearization of the plant by nonlinear feedback and permits to design the PV voltage controller based on a large-signal linear transfer function, removing any possible instability or variation in transient performance caused by the PV source operating point.

The rest of this article is organized as follows. Section II analyzes the influence of the PV source operating point on the stability of the single-phase VSI. Section III establishes the proposed framework for eliminating the possible stability issues using large-signal linearization with the PV power feedforward signal. Section IV presents the results of simulations, including eventual oscillations and instability on the left-hand side of the MPP. Section V reports and comments on experimental results, obtained on a physical hardware setup, with behaviors highly consistent with those emerging in the simulations. A performance comparison with an emerging control scheme from [16] is also provided. Finally, Section VI concludes this article.

II. PV Voltage Control Issues Emerging From Small-Signal Modeling

The switching-cycle averaged model of the system in Fig. 1 is shown in Fig. 2. Here, the VSI power-stage behavior is represented by a current sink, $i_{\mathrm{dc}} = (d_1 - d_2)\, i_{\mathrm{g}}$, and a voltage source, $v_{\mathrm{AB}} = (d_1 - d_2)\, v_{\mathrm{pv}}$, where d_1 and d_2 are the duty cycles of the high-side switches S_1 and S_3, respectively. The filter $L_{\mathrm{f}} = L_{\mathrm{i}} + L_{\mathrm{g}}$ approximates the damped *LCL* filter transfer function, within the bandwidth of interest for the current loop [20]. The power circuit is controlled by a cascaded control loop, where PV-side voltage and current are filtered of the second harmonic, unavoidable in single-phase systems. The outer (slow)

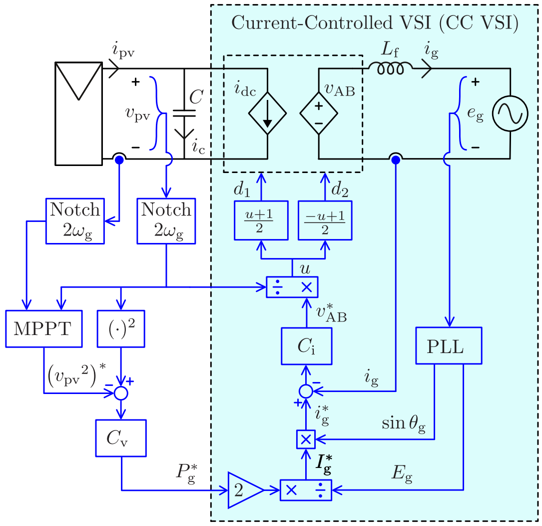

Fig. 2. Average model of the single-stage single-phase PV inverter system.

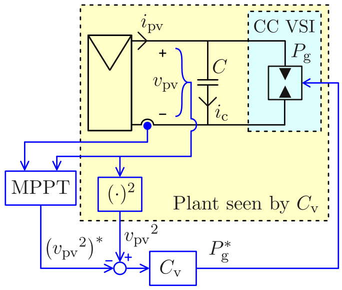

Fig. 3. Simplified model of the single-stage single-phase PV inverter system (current-controlled inverter represented by a constant power load).

PV-voltage loop provides the power reference to the inner (fast) grid-current loop. Typically, the control bandwidth of these loops is 5–10 times apart [21, p. 564], so that the current controller can easily follow the reference provided by the voltage controller. Given the time scale separation between these two loops, the inner current loop appears to be in steady state to the outer voltage loop, and the two loop dynamics are decoupled. As a result, the grid current reference is considered equal to the measured grid current ($i_{\mathrm{g}}^* = i_{\mathrm{g}}$) when designing the outer loop PV voltage controller [22, p. 213], [23]. Assuming the grid voltage and current to be in phase for simplicity, with $\theta_{\mathrm{g}} = \omega_{\mathrm{g}} t$, then

$$e_{\mathrm{g}} = E_{\mathrm{g}} \sin\theta_{\mathrm{g}} \qquad i_{\mathrm{g}} = I_{\mathrm{g}} \sin\theta_{\mathrm{g}} \tag{1}$$

and observing the bottom of Fig. 2, the peak grid-current reference, I_{g}^*, is directly proportional to the active power reference, P_{g}^*, with

$$P_{\mathrm{g}}^* = \tfrac{1}{2} E_{\mathrm{g}} I_{\mathrm{g}}^* \,. \tag{2}$$

Given this proportionality, and since the inner current loop is decoupled from the outer voltage loop, the outer voltage controller, namely C_{v}, sees everything lying downstream of the power reference, P_{g}^*, as an equivalent constant power sink, of value $P_{\mathrm{g}} = P_{\mathrm{g}}^*$. This concept is represented in Fig. 3 (valid for dc components only). Here, P_{g}^* is the output of the PV voltage controller and functions as the control input of the equivalent plant seen by it. This plant is made by the PV source, the interfacing capacitor, and the constant power load representing the current-controlled VSI (CC VSI).

A. Small-Signal PV Voltage Loop Plant Transfer Function

In Fig. 1, the instantaneous power balance equation at the dc-link [24], [25], [26] is

$$p_{\mathrm{pv}} = p_c + p_{\mathrm{dc}} \tag{3}$$

where p_{pv}, p_c, and p_{dc} are the PV source, the dc-link capacitor, and the inverter dc port instantaneous power, respectively. Disregarding losses for simplicity, then p_{dc} is equal to the instantaneous power delivered to the grid, i.e., $p_{\mathrm{dc}} = p_{\mathrm{g}} = e_{\mathrm{g}} i_{\mathrm{g}}$.

Assuming the PV source instantaneous power to be purely dc, indicated as P_{pv}, and using (1), after some algebra, the instantaneous capacitor power in (3) can be written as

$$p_{\mathrm{c}} = \overbrace{P_{\mathrm{pv}} - P_{\mathrm{g}}}^{\text{dc component}} + \overbrace{P_{\mathrm{g}} \cos 2\omega_{\mathrm{g}} t}^{\substack{\text{double frequency} \\ \text{ac component}}} . \tag{4}$$

In (4), the double frequency ac power component, $P_{\mathrm{g}} \cos 2\omega_{\mathrm{g}} t$, is responsible for the ac ripple voltage across the dc-link capacitor, whereas the dc power component, namely

$$P_{\mathrm{c}} = P_{\mathrm{pv}} - P_{\mathrm{g}} \tag{5}$$

is responsible for the change of average value in the dc-link capacitor voltage, and reflects the capacitor's role in buffering temporary power imbalances between the PV source and the grid.

In practical single-stage PV systems, the ac ripple voltage is very small compared with the average component of dc-link capacitor voltage [27]. Therefore, (5) effectively governs the average PV voltage behavior (and the double frequency ac ripple component of the PV voltage is neglected in the following analyses).

Finally, since P_{pv} depends nonlinearly on the PV voltage (cf., Fig. 4), a small-signal linearized version of (5) is traditionally used to derive the PV voltage controller.

In the plant seen by C_{v} in Fig. 3, the small-signal average instantaneous power balance equation is

$$\tilde{P_{\mathrm{pv}}} - \tilde{P_{\mathrm{c}}} = \tilde{P_{\mathrm{g}}}^{*} \tag{6}$$

where $\tilde{P_{\mathrm{pv}}}$ is a linear variation of the PV source average output power, $\tilde{P_{\mathrm{c}}}$ is the average power exchanged by the PV-interfacing capacitor, responsible for the linear increase (or decrease) of the PV voltage, and $\tilde{P_{\mathrm{g}}}^{*}$ is the linear variation of active power injected into the grid. To derive a linear relation between P_{g}^{*} and $v_{\mathrm{pv}}{}^2$, the terms on the left-hand side of (6) are expressed as a function of $\tilde{v_{\mathrm{pv}}}^2$. Considering a generic steady-state operating point in the PV source *I*–*V* curve in Fig. 4, having coordinate (V_{pv} and I_{pv}), it is

$$\tilde{v_{\mathrm{pv}}}^2 = \left.\frac{d(v_{\mathrm{pv}}{}^2)}{dt}\right|_{\substack{V_{\mathrm{pv}} \\ I_{\mathrm{pv}}}} dt = 2V_{\mathrm{pv}} \left.\frac{dv_{\mathrm{pv}}}{dt}\right|_{\substack{V_{\mathrm{pv}} \\ I_{\mathrm{pv}}}} dt = 2V_{\mathrm{pv}} \tilde{v_{\mathrm{pv}}} \tag{7}$$

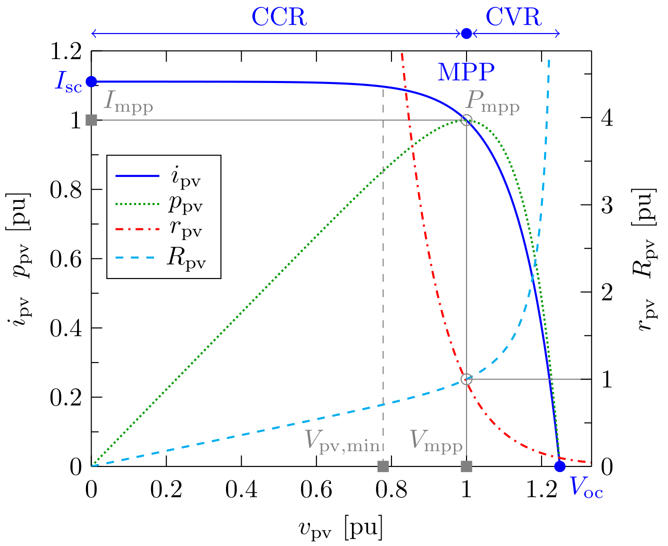

Fig. 4. Typical PV source characteristic curves for PV current (i_{pv}), PV power (p_{pv}), and static and dynamic resistance (R_{pv} and r_{pv}), under standard test conditions of 25 °C temperature and 1kW/m^2 solar irradiation.

and since P_{pv} is a nonlinear function, $P_{\mathrm{pv}} = f(v_{\mathrm{pv}})$, then its linear variation about (V_{pv} and I_{pv}) is expressed as

$$\begin{aligned} \tilde{P_{\mathrm{pv}}} &= \left.\tfrac{d(P_{\mathrm{pv}})}{dt}\right|_{\substack{V_{\mathrm{pv}} \\ I_{\mathrm{pv}}}} dt = \left.\tfrac{d(v_{\mathrm{pv}} i_{\mathrm{pv}})}{dt}\right|_{\substack{V_{\mathrm{pv}} \\ I_{\mathrm{pv}}}} dt \\ &= \left(V_{\mathrm{pv}} \left.\tfrac{di_{\mathrm{pv}}}{dt}\right|_{\substack{V_{\mathrm{pv}} \\ I_{\mathrm{pv}}}} + I_{\mathrm{pv}} \left.\tfrac{dv_{\mathrm{pv}}}{dt}\right|_{\substack{V_{\mathrm{pv}} \\ I_{\mathrm{pv}}}} \right) dt \\ &= -V_{\mathrm{pv}} \left(\tfrac{1}{r_{\mathrm{pv}}} - \tfrac{1}{R_{\mathrm{pv}}} \right) \tilde{v_{\mathrm{pv}}} \end{aligned} \tag{8}$$

where R_{pv} and r_{pv} (see Fig. 4) are the *static resistance* and *dynamic resistance* of the PV source, respectively, defined as [14], [28], [29]

$$R_{\mathrm{pv}} = \frac{V_{\mathrm{pv}}}{I_{\mathrm{pv}}} \qquad r_{\mathrm{pv}} = -\left.\frac{dv_{\mathrm{pv}}}{di_{\mathrm{pv}}}\right|_{\substack{V_{\mathrm{pv}} \\ I_{\mathrm{pv}}}} = -\frac{\tilde{v_{\mathrm{pv}}}}{\tilde{i_{\mathrm{pv}}}}. \tag{9}$$

Notably, R_{pv} and r_{pv} exhibit a wide variation range with respect to the operating point in the *I*–*V* curve of the PV source: in the constant voltage region (CVR) on the right-hand side of the MPP, $R_{\mathrm{pv}} > r_{\mathrm{pv}}$; at the MPP, $R_{\mathrm{pv}} = r_{\mathrm{pv}}$; in the constant current region (CCR) on the left-hand side of the MPP, $R_{\mathrm{pv}} < r_{\mathrm{pv}}$. Substituting V_{pv} obtained from (7) into (8) finally yields

$$\tilde{P_{\mathrm{pv}}} = -\frac{1}{2} \left(\frac{1}{r_{\mathrm{pv}}} - \frac{1}{R_{\mathrm{pv}}} \right) \tilde{v_{\mathrm{pv}}}^2. \tag{10}$$

The instantaneous average power exchanged by the PV-interfacing capacitor can be expressed as the time derivative of the capacitor energy

$$\tilde{P_{\mathrm{c}}} = \dot{\tilde{E_{\mathrm{c}}}} = \tfrac{1}{2} s C \tilde{v_{\mathrm{pv}}}^2 \tag{11}$$

where s represents the Laplace variable. Using (10) and (11) in (6), and rearranging the latter, yields the sought-after small-signal transfer function of the plant seen by the voltage controller in Fig. 3, relating active power reference, P_{g}^{*} (control input), to

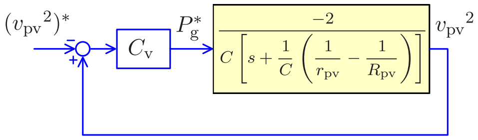

Fig. 5. Block diagram of PV voltage control loop using small-signal transfer function of the PV voltage loop plant, G_{p}, from (12).

squared PV-voltage, $v_{\mathrm{pv}}{}^2$ (output)

$$G_{\mathrm{p}} = \frac{\tilde{v}_{\mathrm{pv}}{}^2}{\tilde{P}_{\mathrm{g}}{}^*} = \frac{-2}{C\left[s+\frac{1}{C}\left(\frac{1}{r_{\mathrm{pv}}}-\frac{1}{R_{\mathrm{pv}}}\right)\right]}. \tag{12}$$

Importantly, the pole in (12) is located at the angular frequency

$$\omega_{\mathrm{p}} = -\frac{1}{C}\left(\frac{1}{r_{\mathrm{pv}}}-\frac{1}{R_{\mathrm{pv}}}\right) \tag{13}$$

which is not constant, given that r_{pv} and R_{pv} exhibit wide variations according to the operating point of the PV source (cf., Fig. 4). There are three possible cases. On the right-hand side of the MPP where $R_{\mathrm{pv}} > r_{\mathrm{pv}}$, (12) is stable given that (13) is in the left-half of the s-plane ($\omega_{\mathrm{p}} < 0$); at the MPP where $R_{\mathrm{pv}} = r_{\mathrm{pv}}$, (12) is marginally stable given that (13) is in $s = 0$ ($\omega_{\mathrm{p}} = 0$); remarkably, on the left-hand side of the MPP where $R_{\mathrm{pv}} < r_{\mathrm{pv}}$, the PV voltage controller sees an unstable plant, since the pole in (13) is in the right-half of the s-plane ($\omega_{\mathrm{p}} > 0$). As studied next, the intrinsic instability of the PV voltage loop plant when the PV source operates on the left-hand side of the MPP complicates the controller design, with dramatic implications for the closed-loop system stability.

B. Pitfalls of Traditional PV Voltage Controller Design

The traditional PV voltage control scheme is reported in Fig. 5, where the inner current loop is considered a unitary constant (therefore, is not shown) since it is much faster than the outer PV voltage loop. Closed-loop stability of the system in Fig. 5 is ensured as long as the poles of

$$\frac{\tilde{v}_{\mathrm{pv}}{}^2}{(\tilde{v}_{\mathrm{pv}}{}^2)^*} = \frac{-C_{\mathrm{v}}G_{\mathrm{p}}}{1-C_{\mathrm{v}}G_{\mathrm{p}}} \tag{14}$$

are in the left-half of the complex plane. Substituting (12) for G_{p}, and adopting a PI voltage controller, with

$$C_{\mathrm{v}} = k_{\mathrm{pv}} + \frac{k_{\mathrm{iv}}}{s} \tag{15}$$

the denominator of (14), namely D, can be written as

$$D = a_2 s^2 + a_1 s + a_0 \tag{16}$$

$$a_2 = C;\quad a_1 = 2k_{\mathrm{pv}} + \left(\frac{1}{r_{\mathrm{pv}}}-\frac{1}{R_{\mathrm{pv}}}\right);\quad a_0 = 2k_{\mathrm{iv}}\,. \tag{17}$$

For (14) to be stable, all coefficients of s in (16) must be positive [30, p. 394]. Since k_{pv}, k_{iv}, C, r_{pv}, and R_{pv} are all positive quantities, then the only condition to be satisfied for closed-loop stability of the PV voltage loop is $a_1 > 0$, true if

$$k_{\mathrm{pv}} > \frac{1}{2}\left(\frac{1}{R_{\mathrm{pv}}}-\frac{1}{r_{\mathrm{pv}}}\right) \tag{18}$$

where R_{pv} and r_{pv} depend on the operating point in the PV source *I–V* characteristic, as shown in Fig. 4. On the right-hand side of the MPP, $r_{\mathrm{pv}} < R_{\mathrm{pv}}$, and at the MPP, $r_{\mathrm{pv}} = R_{\mathrm{pv}}$, and (18) is satisfied since the term on its right-hand side is either negative or zero, respectively. However, on the left-hand side of the MPP, $r_{\mathrm{pv}} > R_{\mathrm{pv}}$, and the terms on either side of (18) are positive; therefore, if the proportional gain is not high enough, condition (18) is violated, making the closed PV voltage loop unstable, with detrimental impact on the inverter's operation.

The worst case to satisfy (18) is when the term on its right-hand side is most positive, occurring when $\frac{1}{R_{\mathrm{pv}}} - \frac{1}{r_{\mathrm{pv}}}$ is highest, i.e., when $R_{\mathrm{pv}} << r_{\mathrm{pv}}$. Observing Fig. 4, this condition occurs in the proximity of the minimum PV operating voltage for the inverter, where $v_{\mathrm{pv}} \cong V_{\mathrm{pv,min}}$ and $i_{\mathrm{pv}} \cong I_{\mathrm{sc}}$, and $\frac{1}{R_{\mathrm{pv}}} = \frac{I_{\mathrm{sc}}}{V_{\mathrm{pv,min}}}$, while $\frac{1}{r_{\mathrm{pv}}} \cong 0$, resulting in

$$k_{\mathrm{pv}} > k_{\mathrm{safety}}\frac{I_{\mathrm{sc}}}{2V_{\mathrm{pv,min}}} = \frac{I_{\mathrm{sc}}}{V_{\mathrm{pv,min}}} \tag{19}$$

where $k_{\mathrm{safety}} = 2$ is a margin chosen to keep k_{pv} away from the value at the edge of instability [15], [16], [31]. In summary, the k_{pv} parameter determines whether the PV voltage loop is stable (or not) on the left-hand side of the MPP.

III. LINEARIZATION USING PV POWER FEEDFORWARD

With the proposed approach, the equivalent plant seen by the voltage controller becomes linear, valid for large signals, and independent of the PV source static and dynamic resistance. The benefit is twofold: the instability condition when the PV source operates on the left-hand side of the MPP is eliminated, and the transient performance of the PV voltage loop no longer depends on the PV source operating point.

Starting from the large-signal version of (6), describing the average power balance on the PV interfacing capacitor

$$P_{\mathrm{pv}} - P_{\mathrm{c}} = P_{\mathrm{g}}^* \tag{20}$$

the only nonlinear term in (20) is P_{pv}, which changes nonlinearly with the PV voltage (cf., power curve in Fig. 4). Subtracting P_{pv} to each side of (20) leads to

$$-P_{\mathrm{c}} = P_{\mathrm{g}}^* - P_{\mathrm{pv}} = -\tfrac{1}{2}C\dot{\overline{v_{\mathrm{pv}}{}^2}} \tag{21}$$

where, on the right-hand side, the average capacitor power is written as a time derivative of the capacitor stored energy. In the Laplace domain, (21) becomes

$$-P_{\mathrm{c}} = -\tfrac{1}{2}sC v_{\mathrm{pv}}{}^2. \tag{22}$$

If "$-P_{\mathrm{c}}$" is now defined to be the new control input to the plant to control, then given that $v_{\mathrm{pv}}{}^2$ is the output state variable, the PV voltage loop plant is represented by the linear large-signal input–output transfer function

$$G_{\mathrm{p1}} = \frac{v_{\mathrm{pv}}^2}{-P_{\mathrm{c}}} = \frac{-2}{sC}\,. \tag{23}$$

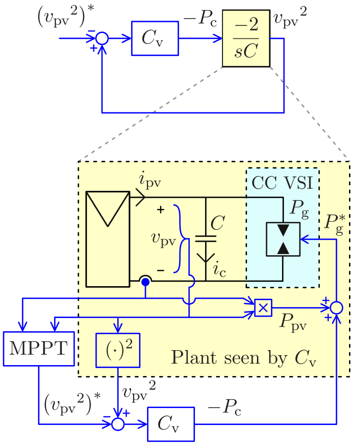

Fig. 6. Block diagram of PV voltage control loop after large-signal linearization (top) and equivalent average model of the system (bottom).

Contrarily to the small-signal transfer function (12), the new plant (23) is independent from the static and dynamic resistance (and, hence, operating point) of the PV source. A simple PI voltage controller, such as (15), can be designed around (23). This controller is tuned considering the block diagram in Fig. 6, representing the dynamics of the outer PV voltage loop, where the controller output is the average capacitor power

$$-P_{\mathrm{c}} = C_{\mathrm{v}} \left(v_{\mathrm{pv}}{}^2 - (v_{\mathrm{pv}}{}^2)^* \right). \tag{24}$$

Since the actual control input to the inner current loop remains the active power reference, P_{g}^*, this is calculated back from (21), adding the average PV power, P_{pv}, to the output of the PV voltage controller, $-P_{\mathrm{c}}$, yielding the new control law for the outer PV voltage loop

$$P_{\mathrm{g}}^* = \overbrace{C_{\mathrm{v}} \left(v_{\mathrm{pv}}{}^2 - (v_{\mathrm{pv}}{}^2)^* \right)}^{\text{PI controller action}} + \overbrace{P_{\mathrm{pv}}}^{\text{feedforward term}} . \tag{25}$$

With the proposed control law (25), closed-loop stability of the PV voltage loop is independent of the PV source operating point. In fact, defining e_{v} as the new state variable, with PV voltage tracking error such that

$$\dot{e_{\mathrm{v}}} = \left(v_{\mathrm{pv}}{}^2 \right)^* - v_{\mathrm{pv}}{}^2 \tag{26}$$

using (15), (25) expressed in the function of the tracking error is

$$P_{\mathrm{g}}^* = -k_{\mathrm{pv}} \dot{e_{\mathrm{v}}} - k_{\mathrm{iv}} e_{\mathrm{v}} + P_{\mathrm{pv}} . \tag{27}$$

Since the PV voltage control loop settles well before the MPPT reference is updated, deriving (26) gives

$$\ddot{e_{\mathrm{v}}} = -\dot{v_{\mathrm{pv}}{}^2} \tag{28}$$

and, finally, plugging (27) and (28) into (21) results in the closed-loop PV voltage error dynamics

$$\tfrac{1}{2} C \ddot{e_{\mathrm{v}}} + k_{\mathrm{pv}} \dot{e_{\mathrm{v}}} + k_{\mathrm{iv}} e_{\mathrm{v}} = 0 \tag{29}$$

which is (large signal) linear and stable, because all its coefficients are positive, and independent of the PV source operating point, as desired.

TABLE I
MAIN PARAMETERS OF PV INVERTER SYSTEM

	Parameter	Variable	Value
PV source (see Fig. 4)	MPP power	P_{mpp}	765 W
	MPP voltage	V_{mpp}	450 V
	MPP current	I_{mpp}	1.7 A
	Open-circuit voltage	V_{oc}	562 V
	Short-circuit current	I_{sc}	1.9 A
Inverter	Grid-side inductance	L_{g}	0.5 mH
	Inverter side inductance	L_{i}	1.5 mH
	Filter capacitance	C_{i}	4.7 µF
	Damping resistance	R_{d}	3.3 Ω
	PV-side capacitance	C	1.19 mF
	Minimum dc input voltage	$V_{\mathrm{pv,min}}$	375 V
	Switching frequency	f_{sw}	10 kHz
Grid	Voltage (rms)	$E_{\mathrm{g}}/\sqrt{2}$	230 V
	Frequency	f_{g}	50 Hz

IV. SIMULATION RESULTS

The PV interfacing grid-connected inverter of Fig. 1 was modeled using PLECS. The main characteristics of the simulated system, reported in Table I, were chosen to match the experimental test setup used for hardware validation.

The inverter synchronizes with the ac grid using a phase-locked loop (PLL) algorithm based on quadrature signal generation [32], suitable for single-phase systems, and implemented as per [33]. The current synthesized by the inverter, in phase with the grid voltage, is controlled by a proportional-resonant current controller, C_{i}, with compensation of third, fifth, and seventh harmonic, having transfer function

$$C_{\mathrm{i}} = k_{\mathrm{pi}} + k_{\mathrm{ri}} \frac{s}{s^2 + \omega_{\mathrm{r}}^2} + \sum_{h=3,5,7} \frac{k_{\mathrm{ri}}}{h} \frac{s}{s^2 + (h\,\omega_{\mathrm{r}})^2} \tag{30}$$

where $\omega_{\mathrm{r}} = 2\pi 50$ rad/s is the resonant angular frequency, $k_{\mathrm{pi}} = 7$ is the proportional gain, $k_{\mathrm{ri}} = 4450$ is the resonant gain, and h is the harmonic order. The third, fifth, and seventh harmonic compensator gains are decreasing with the frequency to avoid eroding the current-loop phase margin (PM) at its cross-over frequency [34], which is $f_{\mathrm{ci}} = 500\,\mathrm{Hz}$. The current controller was designed around the transfer function of the damped *LCL* filter, and the combined time delay of 1.5 sampling intervals due to digital sampling and pulsewidth modulation (PWM) update processes (with one sampling interval being $T_{\mathrm{sw}} = {}^1\!/_{f_{\mathrm{sw}}}$) [35].

The PV voltage controller was designed starting from Fig. 5, assuming the PV source operating at the MPP, and approximating the closed inner current loop to a first-order time delay, of value $T_{\mathrm{d}} = {}^1\!/_{2\pi f_{\mathrm{ci}}}$ (providing a better approximation than a simple unitary gain) [35]. The cross-over frequency of the PV voltage loop was chosen $f_{\mathrm{cv}} = 5\,\mathrm{Hz}$, yielding $k_{\mathrm{pv}} = 1.87 \times 10^{-2}$ and $k_{\mathrm{iv}} = 59 \times 10^{-2}$. Finally, notch filters used on the measured PV voltage and PV current to remove their double frequency component have transfer function [36]

$$H_{\mathrm{notch}} = \frac{s^2 + \omega_o^2}{s^2 + \omega_c s + \omega_o^2} \tag{31}$$

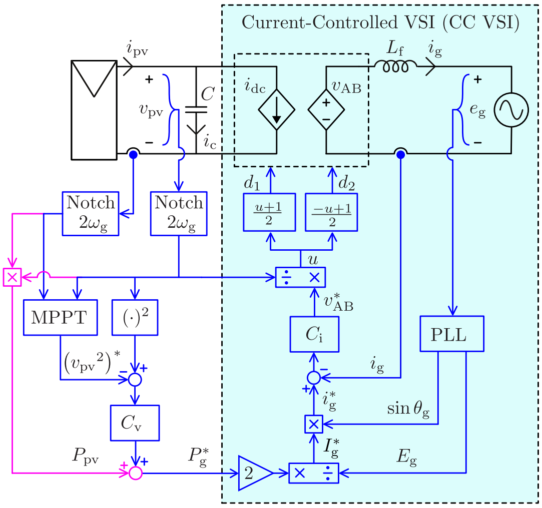

Fig. 7. Average model of the single-stage single-phase PV inverter system. Control scheme using PV power feedforward signal in the voltage loop.

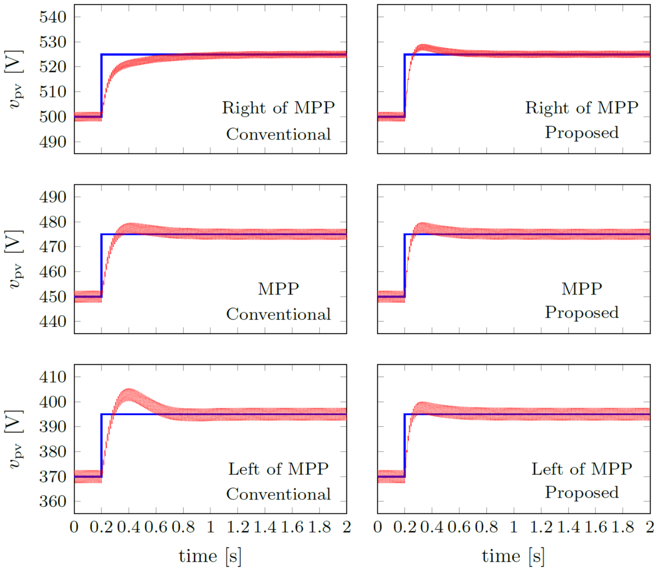

Fig. 8. Simulation results from 25-V PV voltage reference step change, starting from the operating point of the PV source on the right-hand side of MPP, at the MPP, and on the left-hand side of the MPP, with $V_{\mathrm{mpp}} = 450\,\mathrm{V}$. ${v_{\mathrm{pv}}}^2$ regulated by PI controller (left column plots) and by PI controller with PV power feedforward (right column plots).

where ${}^{\omega_o}/_{2\pi} = 100\,\mathrm{Hz}$ is the notch frequency, and ${}^{\omega_c}/_{2\pi} = 85\,\mathrm{Hz}$ is the notch bandwidth. Next, the performance of the control scheme without and with PV power feedforward (see Figs. 2 and 7, respectively) is compared.

A. PV Source Influence on dc Voltage Transient Response

From the plots on the left-hand side of Fig. 8, it is apparent that the step response significantly changes its transient performance across the PV source operating regions when the PV power feedforward is not used. The PV voltage response markedly varies its overshoot and settling time depending on the PV source being on the right-hand side or left-hand side of the MPP.

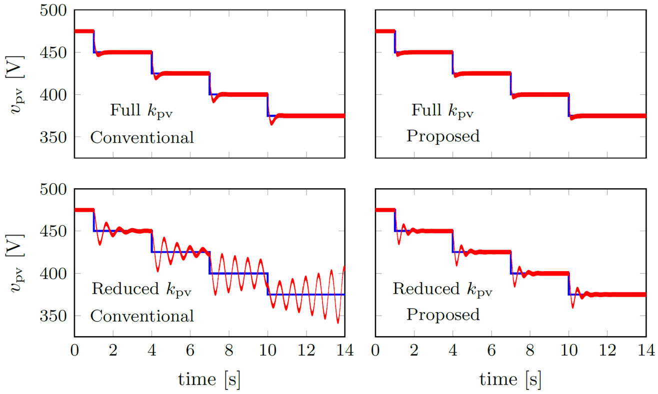

Fig. 9. Simulation results from PV voltage reference sweep from right-hand side to left-hand side of MPP (25 V steps applied every 3 s), with $V_{\mathrm{mpp}} = 450\,\mathrm{V}$. ${v_{\mathrm{pv}}}^2$ regulated by PI controller (left column plots) and by PI controller with PV power feedforward (right column plots).

When the PV power feedforward is added to the output of the PI voltage controller, the plots on the right-hand side of Fig. 8 indicate that the transient response is insensitive to the operating point of the PV source. Settling time and overshoot do not appear to change, regardless of the operating point being located on the right-hand side or left-hand side of the MPP, or at the MPP. In other words, the transient responses show a linear behavior of the voltage loop, eliminating undesired variability of settling time and overshoot.

B. Stability Enhancement Brought by PV Power Feedforward

In Fig. 9, the PV voltage reference is sweeping the operating point of the PV source from the right-hand side to the left-hand side of the MPP. From the top plots in Fig. 9, when the PV voltage controller proportional gain assumes its rated design value, above the limit calculated in (19), both control schemes are stable and perform, as discussed in the previous Section IV-A. With a reduced value of the voltage controller proportional gain, as seen in the bottom plots of Fig. 9, the more the PV source operating point moves to the left-hand side of the MPP, the more underdamped the transient response becomes, until becoming unstable from $t > 10\,\mathrm{s}$. Conversely, the benefit of adding the PV power feedforward signal to the output of the PV voltage PI controller is apparent from the plot at the bottom-right of Fig. 9. Even with a significantly reduced value of proportional gain, the PV voltage loop remains stable, with its transient performance unrelated to the PV source operating point.

Fig. 10 provides an s-domain representation of the PV voltage closed-loop transfer function poles and zeros, for the time-domain tests shown in Fig 9. Two remarks are apparent. First and contrarily to the conventional ${v_{\mathrm{pv}}}^2$ control, with PV power feedforward, the location of closed-loop poles and zeros remains unchanged, leading to dynamics unrelated to the PV source operating point, as is highly desirable.

Second, with a reduced value of proportional gain, the ${v_{\mathrm{pv}}}^2$ control loop response is dictated by two dominant complex-conjugate closed-loop poles. In the case of the conventional controller, these poles eventually move into the right-half plane,

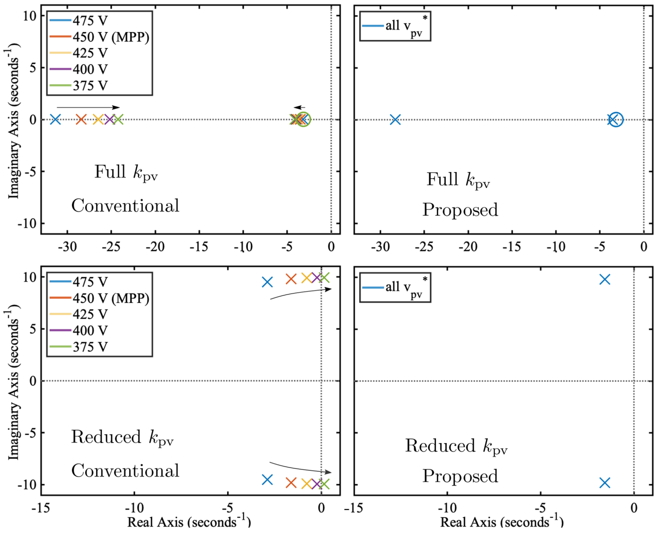

Fig. 10. Pole-zero maps for the PV voltage closed-loop transfer function (× = close-loop pole and ◯ = closed-loop zero), under the test conditions of Fig. 9. $v_{pv}{}^2$ regulated by PI controller (left column plots) and by PI controller with PV power feedforward (right column plots).

explaining underdamped behavior and instability observed in Fig 9.

In addition, the Bode plots in Fig. 11 present the PV voltage loop-gain frequency response under the operating conditions of Fig. 9. Whether the voltage controller proportional gain assumes its full value [see Fig. 11(a)] or a reduced value [see Fig. 11(b)], with the conventional controller, the frequency response is heavily dependent on the PV source operating point. This is evident from the phase plots variation range, leading to a PM degradation as the source moves further to the left-hand side of the MPP, eventually eroding from 32° down to −2°, where the loop is unstable.

With the proposed controller, the outer voltage loop-gain maintains the same magnitude and phase responses regardless of the PV voltage, with a PM equal to 83° and 18° in Fig. 11(a) and (b), respectively, ensuring stability.

Figs. 10 and 11 clarify the essence of the proposed voltage controller with PV power feedforward, yielding time, and frequency responses independent of the PV source operating point.

On the contrary, with conventional control without feedforward, the PV voltage-time and frequency response are operating point dependent, since the plant to control (cf., Fig. 5) has a pole, which undesirably changes its location according to the values of static and dynamic resistance of the PV source, R_{pv} and r_{pv}.

In summary, when the operating point of the PV source moves to the left-hand side of the MPP, such as during power curtailment operation or rapid changes in irradiance, the algorithm using PV power feedforward provides a critical stability enhancement.

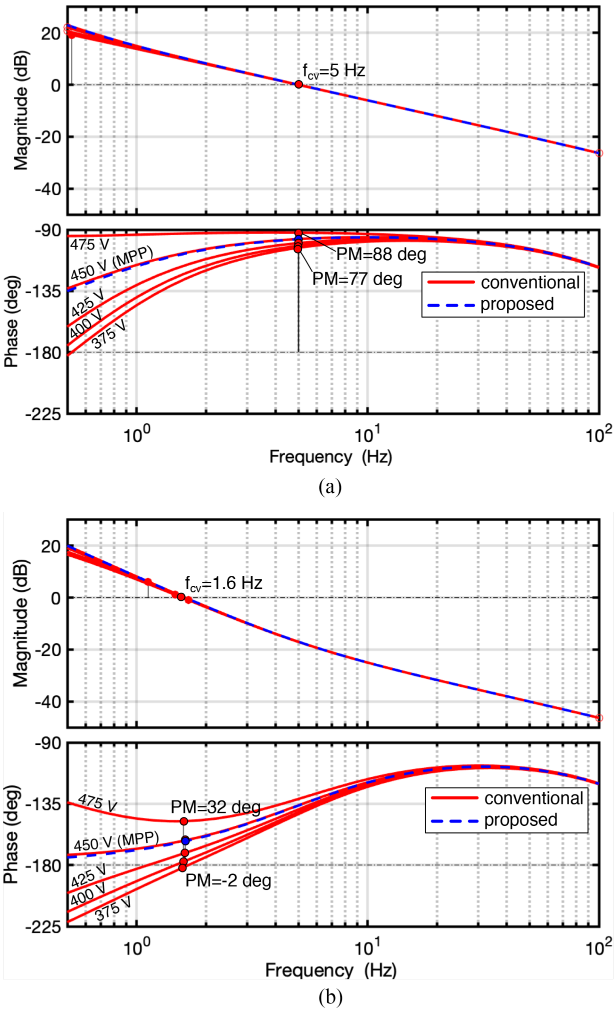

Fig. 11. Outer voltage loop-gain Bode plots with conventional and proposed $v_{pv}{}^2$ controller, under test conditions of Fig. 9. (a) Bode plots with full k_{pv}. (b) Bode plots with reduced k_{pv}.

V. Experimental Results and Discussion

To consolidate the theoretical investigation and the behavior emerging from the simulation results, a hardware-based lab setup was designed and built. The PV source was replaced by a Magna-Power PV Emulator model SL800-7.5/415+HS, and the inverter was a Danfoss FC-302P2K2 (a three-phase inverter rated 2.2 kW, however, two of the three switching legs were used to operate it as a single-phase inverter). The inverter was interfaced via custom-designed measurement and protection interfaces to a digital microcontroller platform, based on Texas Instruments F28379D. The inverter power output was then connected to an NHR grid emulator model 9410-12, via a damped *LCL* filter and an isolation transformer, the latter being used for safety purposes and to decouple the grid emulator ground from the inverter output. A simplified schematic of the lab setup is represented in Fig. 12(a), while a photo is reported in Fig. 12(b). The elements in the experimental setup have the same parameters used in the simulations, reported in Table I.

A. PV Voltage Step Response Experiments

In the first set of experiments, the PV voltage step response was tested with the PV source operating on the right-hand side of the MPP [see Fig. 13(a) and (b)], at the MPP [see Fig. 13(c)

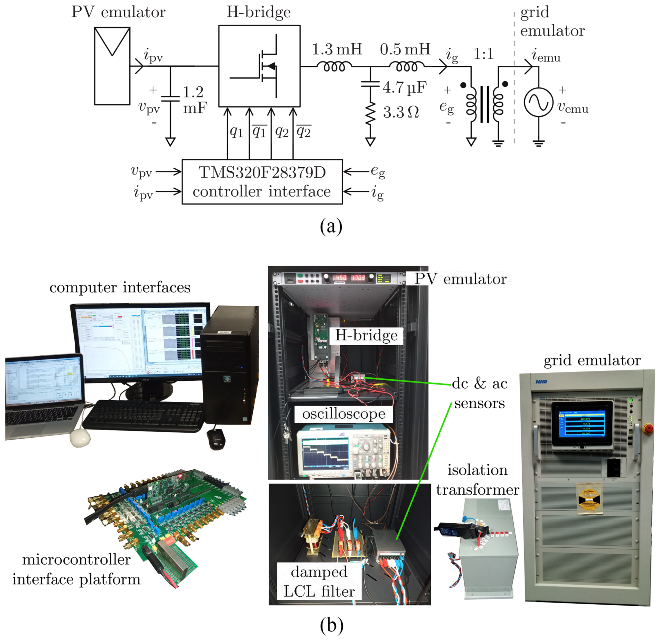

(a)

(b)

Fig. 12. Hardware test setup. (a) Schematic diagram. (b) Photograph.

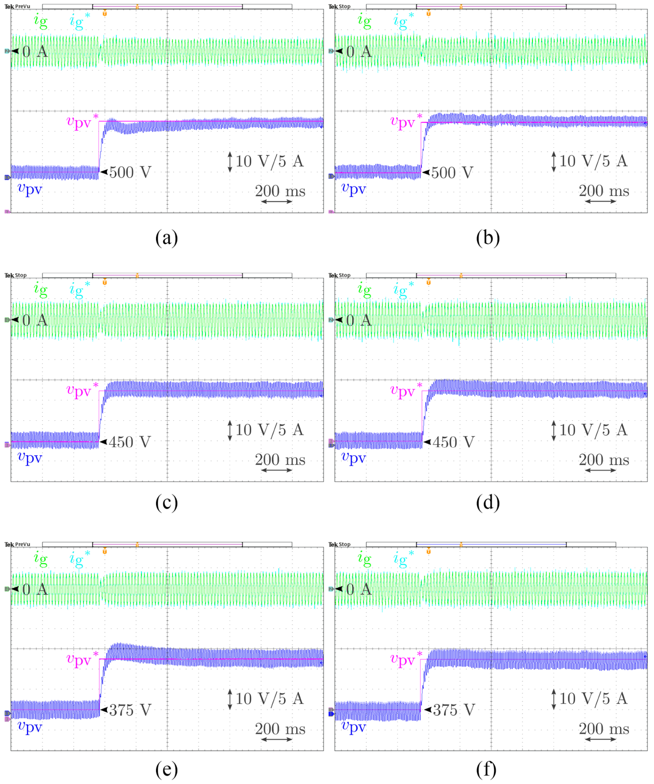

(a) (b)

(c) (d)

(e) (f)

Fig. 13. Measured PV voltage response for a 25-V step change in reference. Without PV power feedforward: (a) right-hand side of MPP, (b) MPP, and (c) left-hand side of MPP. With PV power feedforward: (d) right-hand side of MPP, (e) MPP, and (f) Left-hand side of MPP. (Note: $V_{\text{mpp}} = 450\,\text{V}$).

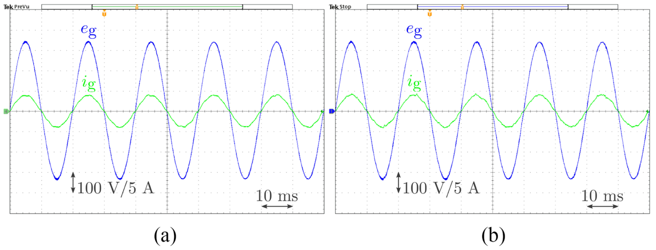

(a) (b)

Fig. 14. Measured grid voltage and grid current with PV source at MPP. Outer voltage loop (a) without PV power feedforward and (b) with PV power feedforward.

and (d)], and on the left-hand side of the MPP [see Fig. 13(e) and (f)].

Without PV power feedforward signal, the step response dynamic performance undesirably depends on the PV source operating point. As shown in Fig. 13(a) (right-hand side of the MPP), the settling time is very large and the response appears overdamped. While the response appears ideal in Fig. 13(c) (MPP), the PV voltage visibly overshoots the reference input in Fig. 13(e) (left-hand side of MPP). Conversely, when the PV power feedforward signal is used, the PV voltage response presents a consistent transient performance, regardless of whether the PV source operates, [cf., Fig. 13(b)] (right-hand side of MPP), Fig. 13(d) (MPP) and Fig. 13(f) (left-hand side of MPP). The plots in Fig. 13 remark that the PV power feedforward signal added to the output of the PI controller has the effect of linearizing the PV voltage loop, decoupling the transient response quality from the PV source operating point. While there is no substantial difference in the current synthesized by the inverter (cf., Fig. 14), if the PV power feedforward signal is not used, then the behavior of the voltage loop is dependent on the PV source. In particular, on the right-hand side of the MPP, the response becomes slow and overdamped, and on the left-hand side of the MPP the PV voltage step response becomes undesirably underdamped. While this matter does not impact the converter stability if the outer voltage loop controller gains are appropriately chosen, severe instability scenarios can emerge if the value of the PV voltage controller proportional gain is not high enough, as proven next.

B. Enhancement of PV Voltage Stability Experiments

In the second set of experiments, the PV voltage reference was progressively decreased in steps of 25 V, gradually bringing the operating point of the PV source from the right-hand side to the left-hand side of the MPP. This test is run first with the rated value of the PV voltage controller proportional gain, then with a reduced gain value [yet above the stability limit of (18)], and finally with a proportional gain value below the stability limit of (18). In addition to the comparison between the performance of the outer loop controlled without and with PV power feedforward, a technique from the literature [16] addressing control of $v_{\text{pv}}{}^2$ to enhance PV voltage stability was assessed and implemented. This technique is based on the idea that the PV voltage loop plant in Fig. 5, i.e., (12), has the dimension of an impedance, with an unstable pole when the PV source operates on the left-hand side of the MPP. Hence, a *virtual admittance* term (Y_{v}) is added in the control loop to remove the plant instability, as per Fig. 15. From this figure, after some algebra, the equivalent PV voltage

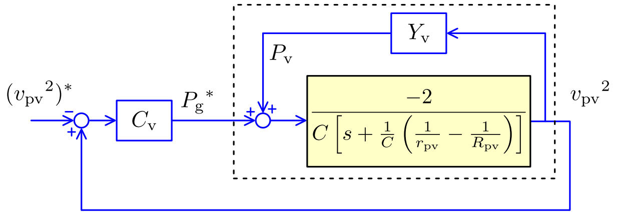

Fig. 15. Principle of $v_{\rm pv}{}^2$ control with stabilizing virtual admittance $Y_{\rm v}$ [16].

loop plant inside dashed lines is

$$G_{\rm pY_v} = \frac{\tilde{v_{\rm pv}{}^2}}{\tilde{P}_{\rm g}{}^*} = \frac{-2}{C\left[s+\frac{1}{C}\left(\frac{1}{r_{\rm pv}}-\frac{1}{R_{\rm pv}}+2\,Y_{\rm v}\right)\right]} \tag{32}$$

with $r_{\rm pv}$ and $R_{\rm pv}$ the operating point dependent variables (cf., Section II-A). $Y_{\rm v}$ needs to be *chosen* so that on the left-hand side of the MPP, where $r_{\rm pv} > R_{\rm pv}$, the pole in (32) remains on the right-half plane (for a stable plant); hence, in general

$$\min\left\{\frac{1}{r_{\rm pv}}-\frac{1}{R_{\rm pv}}\right\}+2\,Y_{\rm v}>0 \tag{33}$$

and a possible conservative rule of thumb is to choose

$$Y_{\rm v} = \frac{I_{\rm sc}}{2V_{\rm pv,min}}. \tag{34}$$

It is noteworthy recognizing few important points about the virtual admittance technique of [16]: the output of the virtual admittance branch ($P_{\rm v}$ in Fig. 15) has also a dimension of power, and acts as a power feedforward term to the output of the voltage controller, however its value is determined by $Y_{\rm v}$; the technique is derived in [16] on the basis of small-signal analysis, as a result, the dependence on the operating point is not removed; while [16] does not provide hardware-based results, they are provided in this article for the first time.

Fig. 16(a), (d), and (g) display the results of the PV voltage reference sweep from right-hand side to left-hand side of the MPP as the value of the voltage controller proportional gain is progressively reduced, and the PV power feedforward compensation is not used. Clearly, the lower the value of the proportional gain, the lower the stability margin is: the PV voltage regulation becomes increasingly more underdamped and eventually unstable on the left-hand side of the MPP [see Fig. 16(g)]. The instability is also noticeable by the grid current envelope in the latter figure, exhibiting increasingly wider oscillations. Fig. 16(d) and (g) are particularly important because, other than the eventual instability, they illustrate the damping degradation phenomenon as the PV voltage reference is swept to the left-hand side of the MPP.

On the other hand, the results in Fig. 16(b), (e), and (h) display the results with PV power feedforward signal added to the output of the PI voltage controller to cancel the influence of the PV source. The patterns visible from these figures confirm that the PV power feedforward signal is decisive in maintaining stability, even when the proportional gain of the voltage controller is low. Furthermore, observing Fig. 16(b), (e), and (h) each individually, it is noticeable that as the PV source operating point is progressively swept to the left-hand side of the MPP, the PV voltage transient performance does not change. This response is determined by the choice of proportional gain value only, rather than by the operating point of the PV source, confirming that the nonlinearity induced by the PV generator is canceled. This outcome is exactly opposite to the behavior displayed in Fig. 16(a), (d), and (g), for PV voltage control without PV power feedforward, where the more the PV voltage moves toward the left-hand side of the MPP, the more underdamped the response becomes. Except for the greater damping displayed in the experiments, likely due to unmodeled parasitic resistive elements, the experimental results accurately match the behaviors that emerged from the simulations and were expected from the theory. Without PV power feedforward, the control of $v_{\rm pv}{}^2$ is affected by the PV source and can become unstable on the left of the MPP, while such vulnerabilities are eliminated when adopting the PV power feedforward signal.

In addition, the same tests were repeated with the virtual admittance emulation control scheme of Fig. 15 (adapted from [16]), with $Y_{\rm v}$ from (34) and associated results shown in Fig. 16(c), (f), and (i). While this control scheme also effectively removed the PV voltage instability, Fig. 16(f) and (i) confirm that the transient performance remains undesirably coupled to the PV source operating point. In the latter figures, overshoot and settling time vary widely as the PV voltage decreases, flagging that the PV source nonlinearity maintains an unwanted influence on the PV voltage regulation.

C. Features Comparison of dc Voltage Control Schemes Tested

At last, a feature comparison of the techniques experimentally tested in this work is presented in Fig. 17. While the *Stability* disadvantages of using a conventional PI controller have been extensively discussed, it is worth noting that the virtual admittance scheme has the advantage of not requiring a PV current sensor, thus the high score under *economy* in Fig. 17. The proposed control with PV power feedforward requires a PV current sensor; however, this could easily be already adopted for MPPT purposes, since most popular techniques, such as perturb and observe or incremental conductance [9], require measuring PV voltage and PV current.

Transient performance of the virtual admittance scheme is also undesirably susceptible to the PV source operating point; hence, the lower score in Fig. 17 compared with the proposed PV power feedforward, whose transient performance is determined at the design stage, is decoupled from the PV source and valid for large signals.

Controller *tuning simplicity* for the proposed scheme is also higher than others, as the PV voltage loop plant is simply determined by the dc-link capacitor (cf., Fig. 6), and there is no *additional designer input* required. Conversely, with the virtual admittance technique, the designer must additionally choose the value of virtual admittance, $Y_{\rm v}$, which requires knowledge of PV source and inverter parameters.

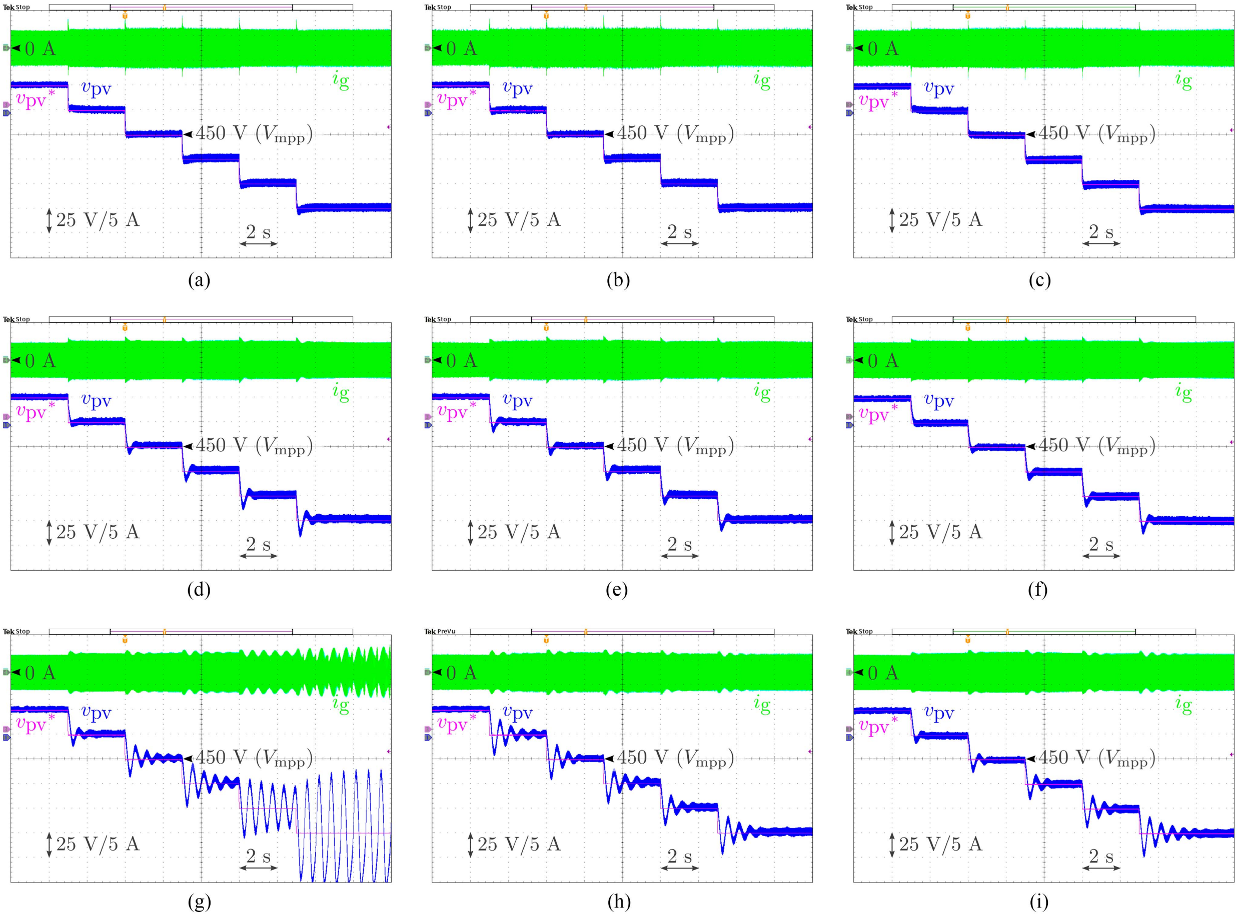

Fig. 16. Measured PV voltage response for 25 V decreasing reference step changes applied every 3 s. (a) Rated k_{pv}, without feedforward. (b) Rated k_{pv}, with feedforward. (c) Rated k_{pv}, with virtual admittance. (d) k_{pv} reduced by 70%, without feedforward. (e) k_{pv} reduced by 70%, with feedforward. (f) k_{pv} reduced by 70%, with virtual admittance. (g) k_{pv} reduced by 90%, without feedforward. (h) k_{pv} reduced by 90%, with feedforward. (i) k_{pv} reduced by 90%, with virtual admittance.

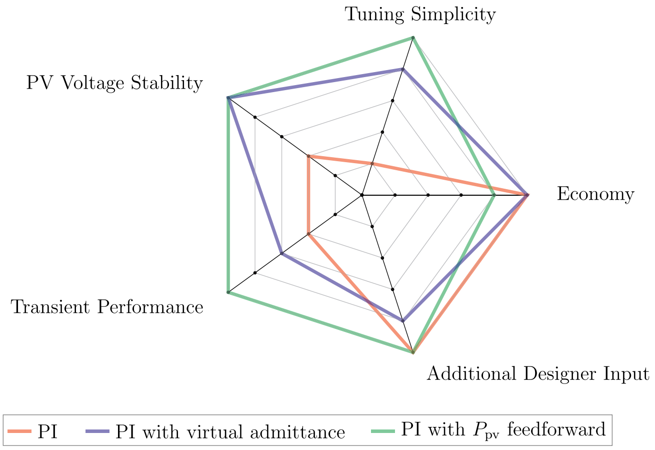

Fig. 17. Features comparison of $v_{pv}{}^2$ control schemes experimentally tested in this paper (outermost contour = most desirable).

VI. Conclusion

This article investigated PV voltage control issues in the single-stage grid-connected inverter. When designing a controller based on small-signal analysis, it was found that the PV source causes a right-half-plane pole to appear in the PV voltage loop plant transfer function, when the operating point of the PV source is on the left-hand side of the MPP. This matter significantly challenges the design of the voltage controller, to the point where if the proportional gain is below a set threshold given in this article, the outer voltage loop becomes unstable on the left-hand side of the MPP. In contrast, adding the PV power feedforward signal to the output of the PV voltage controller cancels the nonlinearity and possible instability induced by the PV source, desirably linearizing the PV voltage regulation loop performance.

A technique from the literature based on virtual admittance emulation was then rigorously described and hardware tested for the first time. This technique also cancels the possible instability at the left-hand side of the MPP, with the advantage of not using a PV current sensor, outweighed by the weaknesses of a PV source-influenced transient performance, and increased tuning and design complexity.

The key takeaway of this research is twofold. First, it is advisable to adopt the PV power feedforward signal to avoid altogether possible instability of the PV voltage control loop. Second, if the proposed PV power feedforward scheme or virtual admittance schemes are not adopted, then tuning the PV voltage controller must be carried out extremely carefully, as a low value of proportional gain may lead to converter instability on the left-hand side of the MPP, occurring for instance during PV power curtailment operation or rapid changes in solar irradiance.

REFERENCES

[1] International Renewable Energy Agency (IRENA), "Grid codes for renewable powered systems," Abu Dhabi, UAE, Tech. Rep. 2022, [Online]. Available: www.irena.org/publications

[2] *Grid Connection of Energy Systems via Inverters*. Part 2: Inverter Requirements Standard New Zealand AS 4777.2, 2020.

[3] IEEE standard for interconnection and interoperability of distributed energy resources with associated electric power systems interfaces, Standard IEEE 1547, 2018.

[4] Generators connected to the low-voltage distribution network. Technical requirements for the connection to and parallel operation with low-voltage distribution networks, (English translation of VDE-AR-N 4105, 2018-11), Standard VDE-AR-N 4105:2018-11, 2018.

[5] Reference technical rules for the connection of active and passive users to the LV electrical utilities (in Italian), Standard CEI 0-22, Apr. 2022. [Online]. Available: https://www.ceinorme.it/doc/norme/18309.pdf

[6] H. D. Tafti et al., "Extended functionalities of photovoltaic systems with flexible power point tracking: Recent advances," *IEEE Trans. Power Electron.*, vol. 35, no. 9, pp. 9342–9356, Sep. 2020.

[7] X. Li, H. Wen, B. Chen, S. Ding, and W. Xiao, "A cost-effective power ramp rate control strategy based on flexible power point tracking for photovoltaic system," *Sol. Energy*, vol. 208, pp. 1058–1067, 2020.

[8] D. Sera, R. Teodorescu, J. Hantschel, and M. Knoll, "Optimized maximum power point tracker for fast-changing environmental conditions," *IEEE Trans. Ind. Electron.*, vol. 55, no. 7, pp. 2629–2637, Jul. 2008.

[9] D. Sera, L. Mathe, T. Kerekes, S. V. Spataru, and R. Teodorescu, "On the perturb-and-observe and incremental conductance MPPT methods for PV systems," *IEEE J. Photovolt.*, vol. 3, no. 3, pp. 1070–1078, Jul. 2013.

[10] W. Xiao, W. G. Dunford, P. R. Palmer, and A. Capel, "Regulation of photovoltaic voltage," *IEEE Trans. Ind. Electron.*, vol. 54, no. 3, pp. 1365–1374, Jun. 2007.

[11] J. Viinamäki, J. Jokipii, T. Messo, T. Suntio, M. Sitbon, and A. Kuperman, "Comprehensive dynamic analysis of photovoltaic generator interfacing DC-DC boost power stage," *IET Renewable Power Gener.*, vol. 9, no. 4, pp. 306–314, 2015.

[12] A. Kuperman, M. Sitbon, S. Gadelovits, M. Averbukh, and T. Suntio, "Single-source multi-battery solar charger: Analysis and stability issues," *Energies*, vol. 8, no. 7, pp. 6427–6450, 2015.

[13] S. Kolesnik, M. Sitbon, S. Gadelovits, T. Suntio, and A. Kuperman, *Renew. Sustain. Energy Rev.*, vol. 51, pp. 1771–1783, Nov. 2015.

[14] L. Nousiainen et al., "Photovoltaic generator as an input source for power electronic converters," *IEEE Trans. Power Electron.*, vol. 28, no. 6, pp. 3028–3038, Jun. 2013.

[15] T. Messo, J. Jokipii, J. Puukko, and T. Suntio, "Determining the value of DC-link capacitance to ensure stable operation of a three-phase photovoltaic inverter," *IEEE Trans. Power Electron.*, vol. 29, no. 2, pp. 665–673, Feb. 2014.

[16] A. Urtasun, P. Sanchis, and L. Marroyo, "DC capacitance reduction in three-phase photovoltaic inverters by using virtual impedance emulation," in *Proc. 21st Eur. Conf. Power Electron. Appl.*, 2019, pp. 1–9.

[17] A. Urtasun, P. Sanchis, and L. Marroyo, "DC capacitance reduction in photovoltaic inverters based on PV voltage feed-forward compensation," in *Proc. IEEE Int. Conf. Environ. Elect. Eng. Ind. Commercial Power Syst. Eur.*, 2021, pp. 1–6.

[18] M. M. Rahman and Y. A.-R. I. Mohamed, "Dynamic analysis and active stabilization of a utility-scale grid-connected current-source inverter-based PV system considering source dynamics," *IEEE Trans. Power Syst.*, vol. 37, no. 6, pp. 4590–4604, Nov. 2022.

[19] S. Kouro, B. Wu, H. Abu-Rub, and F. Blaabjerg, *Power Electronics for Renewable Energy Systems, Transportation and Industrial Applications*. Chichester, U.K.: Wiley, 2014.

[20] M. Liserre, F. Blaabjerg, and S. Hansen, "Design and control of an LCL-filter-based three-phase active rectifier," *IEEE Trans. Ind. Appl.*, vol. 41, no. 5, pp. 1281–1291, Sep./Oct. 2005.

[21] T. Suntio, T. Messo, and J. Puukko, *Power Electronic Converters: Dynamics and Control in Conventional and Renewable Energy Applications*. Weinheim, Germany: Wiley, 2018.

[22] R. Teodorescu, M. Liserre, and P. Rodriguez, *Grid Converters for Photovoltaic and Wind Power Systems*. Piscataway, NJ, USA: Wiley, Jan. 2011.

[23] R. A. Mastromauro, M. Liserre, and A. Dell'Aquila, "Control issues in single-stage photovoltaic systems: MPPT, current and voltage control," *IEEE Trans. Ind. Informat.*, vol. 8, no. 2, pp. 241–254, May 2012.

[24] Y.-M. Chen, C.-H. Chang, and H.-C. Wu, "DC-link capacitor selections for the single-phase grid-connected PV system," in *Proc. IEEE Int. Conf. Power Electron. Drive Sys.*, 2009, pp. 72–77.

[25] Y.-M. Chen, H.-C. Wu, Y.-C. Chen, K.-Y. Lee, and S.-S. Shyu, "The AC line current regulation strategy for the grid-connected PV system," *IEEE Trans. Power Electron.*, vol. 25, no. 1, pp. 209–218, Jan. 2010.

[26] N. E. Zakzouk, A. K. Abdelsalam, A. A. Helal, and B. W. Williams, "PV single-phase grid-connected converter: DC-link voltage sensorless prospective," *IEEE Trans. Emerg. Sel. Topics Power Electron.*, vol. 5, no. 1, pp. 526–546, Mar. 2017.

[27] F. El Aamri et al., "Stability analysis for DC-link voltage controller design in single-stage single-phase grid-connected PV inverters," *IEEE J. Photovolt.*, early access, Apr. 12, 2023, doi: 10.1109/JPHOTOV.2023.3263253.

[28] L. Callegaro, M. Ciobotaru, D. J. Pagano, and J. E. Fletcher, "Feedback linearization control in photovoltaic module integrated converters," *IEEE Trans. Power Electron.*, vol. 34, no. 7, pp. 6876–6889, Jul. 2019.

[29] L. Callegaro, C. A. Rojas, M. Ciobotaru, and J. E. Fletcher, "A controller improving photovoltaic voltage regulation in the single-stage single-phase inverter," *IEEE Trans. Power Electron.*, vol. 37, no. 1, pp. 354–363, Jan. 2022.

[30] R. Dorf and R. Bishop, *Modern Control Systems*, 12th ed., Upper Saddle River, NJ, USA: Pearson Prentice Hall, 2011.

[31] J. W. Kolar et al., "Conceptualization and multi-objective optimization of the electric system of an airborne wind turbine," in *Proc. IEEE Int. Symp. Ind. Electron.*, 2011, pp. 32–55.

[32] M. Ciobotaru, R. Teodorescu, and F. Blaabjerg, "A new single-phase PLL structure based on second order generalized integrator," in *Proc. 37th IEEE Power Electron. Specialists Conf.*, 2006, pp. 1–6.

[33] Texas Instruments Inc., "Software phase locked loop design using C2000 microcontrollers for single phase grid connected inverter," Dallas, TX, USA, Appl. Rep. SPRABT3A, Jul. 2017. [Online]. Available: https://www.ti.com/lit/an/sprabt3a/sprabt3a.pdf

[34] M. Schiesser, S. Wasterlain, M. Marchesoni, and M. Carpita, "A simplified design strategy for multi-resonant current control of a grid-connected voltage source inverter with an LCL filter," *Energies*, vol. 11, no. 3, 2018, Art. no. 609.

[35] S. Buso and P. Mattavelli, *Digital Control in Power Electronics*, 2nd ed. San Rafael, CA, USA: Morgan & Claypool, 2015.

[36] M. Simões and F. Farret, *Modeling Power Electronics and Interfacing Energy Conversion Systems*. Hoboken, NJ, USA: Wiley, 2016.

Leonardo Callegaro (Member, IEEE) received the B.Eng. and M.Eng. (Hons.) degrees from the University of Padova, Padova, Italy, in 2004 and 2006, respectively, and the Ph.D. degree from the University of New South Wales, Sydney, NSW, Australia, in 2018, all in electrical engineering.

He is currently a Lecturer in electrical engineering at Macquarie University, Sydney, NSW, Australia. His research interests include modeling and control for power electronics in photovoltaic energy systems, microgrids, electric transportation, grid integration of renewables, and more.

Foad Taghizadeh (Senior Member, IEEE) received the Ph.D. degree in electrical engineering from Macquarie University, Sydney, NSW, Australia, in 2018.

He is currently a Lecturer with the School of Engineering, Macquarie University. His research interests include electric vehicle chargers, control systems, microgrid and distributed energy system integration, power quality, and energy storage systems.

Sara Deilami (Senior Member, IEEE) received the Ph.D. degree in electrical and power engineering from Curtin University, Perth, WA, Australia.

She is currently a Senior Lecturer with the School of Engineering, Macquarie University, Sydney, NSW, Australia, where she is also the Associate Director of Smart Grid Cities (SGC). Her research interests include grid integration, including electric vehicle charging, wireless technology, renewable energy integration, power quality, and power system protection.

Dr. Deilami is the Vice Chair of IEEE Power and Energy Society (PES) in NSW Section.

Mihai Ciobotaru (Senior Member, IEEE) received the Engineering Diploma and M.Eng. degree from the University of Galati, Galati, Romania, in 2002 and 2003, respectively, and the Ph.D. degree from Aalborg University, Aalborg, Denmark, in 2009, all in electrical engineering.

He is currently an Adjunct Fellow with Macquarie University, Sydney, NSW, Australia, and the Principal R&D Engineer with EcoJoule Energy, Brisbane area, QLD, Australia. His research interests include distributed energy resources, power electronic converters, battery energy storage systems, and ac and dc microgrids.